Materials Advances

ROYAL SOCIETY OF CHEMISTRY

PAPER

View Article Online
View Journal | View Issue

Check for updates

Cite this: *Mater. Adv.*, 2024, 5, 8927

Synergistic effects of astragalus on 3D-printed calcium silicate/poly-ε-caprolactone scaffolds to regulate inflammation/osteogenesis for bone regeneration

Jian-Jr Lee,†[ab] Yen-Hong Lin,†[c] Ting-You Kuo,[d] Alvin Kai-Xing Lee,[e] Cheng-Yu Chen*[c] and Ming-You Shie *[cfg]

Bone defects represent a significant clinical challenge, traditionally addressed primarily through scaffold-based repair strategies. However, recent studies have revealed that relying solely on scaffolds may not fully overcome the bottlenecks in bone defect repair. Mounting evidence suggests that modulating the inflammatory response plays a crucial role in the bone healing process. While moderate inflammation can promote bone tissue regeneration, excessive or prolonged inflammatory responses may impede the repair process. Our previously developed calcium silicate (CS) scaffold, known to stimulate osteoblast proliferation and accelerate bone tissue formation, was enhanced with magnesium–strontium to boost cellular biological activity and foster bone formation and angiogenesis. In this study, the effects of 3D-printed CS scaffolds reinforced with astragalus (Ast) on inflammation regulation and osteogenic gene expression were examined. X-ray diffraction and Fourier transform infrared spectroscopy confirmed that the Ast phase structure and chemical functional groups were added to the materials. The findings revealed that integrating Ast improves scaffold biocompatibility, bioactivity, and bone and vascular tissue formation efficacy, enhances mechanical strength, and decelerates biodegradation. The 5% Ast-containing CS scaffold exhibited superior capabilities in promoting cell proliferation and differentiation, indicative of effective bone regeneration. Moreover, analysis of hMSC-seeded AstCS scaffold supernatants revealed significantly reduced levels of pro-inflammatory cytokines IL-1β and IL-6, coupled with elevated expression of the anti-inflammatory factor IL-1RA. These results suggest that Astragalus incorporation effectively modulates inflammatory signaling in the scaffold microenvironment. Transcriptome RNA sequencing revealed that this scaffold modulated multiple signaling pathways crucial for bone regeneration, such as *WNT*, *AKT*, and *PI3K*, and significantly influenced genes associated with cellular bone regeneration, angiogenesis, and immune responses. These results highlight the potential of combining Ast with CS in 3D-printed scaffolds for bone tissue engineering, offering new strategies for employing natural pharmaceutical ingredients as bioactivity enhancers and providing a substantial foundation for designing future bone regeneration materials with immune-modulating capabilities.

Open Access Article. Published on 15 October 2024. Downloaded on 2/12/2026 7:52:48 PM.
This article is licensed under a Creative Commons Attribution-NonCommercial 3.0 Unported Licence.

Received 24th May 2024,
Accepted 10th October 2024

DOI: 10.1039/d4ma00531g

rsc.li/materials-advances

1. Introduction

The healing of large-scale bone fractures and critical-size bone defects presents significant challenges in the natural repair process, necessitating the use of substitutes such as autografts or bone grafts to assist in bone healing. However, optimal treatment outcomes have always been a clinical challenge in orthopedics.[1–3] A notable deficiency is the lack of suitable regenerative materials for the rapid repair of extensive bone defects in clinical settings.[4] Research in the field of bone tissue engineering has been predominantly focused on the effective use of materials to construct scaffolds that facilitate rapid bone induction and conduction. These scaffolds have been

[a] *School of Medicine, China Medical University, Taichung 406040, Taiwan*
[b] *Department of Plastic and Reconstructive Surgery, China Medical University Hospital, Taichung City, 404332, Taiwan*
[c] *Research & Development Center for x-Dimensional Extracellular Vesicles, China Medical University Hospital, Taichung 404332, Taiwan. E-mail: eric@mail.cmu.edu.tw*
[d] *Graduate Institute of Biomedical Sciences, China Medical University, Taichung 406040, Taiwan*
[e] *Department of Orthopedics, China Medical University Hospital, Taichung 404332, Taiwan*
[f] *Department of Biomedical Engineering, China Medical University, Taichung 406040, Taiwan*
[g] *Department of Bioinformatics and Medical Engineering, Asia University, Taichung 41354, Taiwan*
† Both authors contributed equally to this work.

© 2024 The Author(s). Published by the Royal Society of Chemistry

Open Access Article. Published on 15 October 2024. Downloaded on 2/12/2026 7:52:48 PM.
This article is licensed under a Creative Commons Attribution-NonCommercial 3.0 Unported Licence.

engineered to gradually release components that promote bone tissue integration or stem cell absorption during prolonged bone healing.[5–7] Ideal synthetic bone grafts should exhibit biodegradability, biocompatibility, osteogenesis, and antibacterial activity.[8] Currently, calcium phosphate bone cement is the preferred option for bone grafts because it mimics the major inorganic component of the bone tissue, is bioactive, and can form intimate and functional interfaces with the natural bone.[9–11]

Commonly used clinical materials for bone defects include hydroxyapatite, calcium silicate, tricalcium phosphate, and bioglass.[12] Hydroxyapatite mimics the bone's natural inorganic phase and are widely used in the fabrication of scaffolds as biological materials. Other materials with similar properties include chitosan, gelatin, polyethylene glycol, and polylactic acid. However, most bone transplant substitutes, typically synthetic ceramics and cement, lack inherent bone-inductive properties and require additional materials to stimulate bone induction.[13] Calcium silicate (CS) is an essential element in bone development, and cellular compatibility with highly biocompatible materials is required to initiate the bone regeneration pathway.[14–16] Our team has long been dedicated to utilizing 3D printing to customize various porous bioceramic scaffolds that successfully promote tissue regeneration, including diverse forms such as magnesium–strontium, red sage–CS, and γ-polyglutamic acid–CS. 3D printing technology has demonstrated numerous unique advantages in regenerative medicine.[17–20] Customized structural design addresses irregular and large-area injuries in clinical settings, whereas applying multiple materials allows the designed scaffold to possess diverse functionalities.[21,22] This study used fused deposition modelling printing technology to construct a bioceramic scaffold. We aimed to further explore the intricate association between anti-inflammation and bone regeneration.

Many studies in the past have used surface modification or mixing of natural products as a way to improve the immune response induced by bone grafts.[22–25] Astragalus (Ast), a well-known mild herb, has gained popularity as a health supplement in recent years due to its ability to balance the body's weight and blood circulation and treat conditions such as chronic fatigue, wounds, anemia, loss of appetite, weakness, and fever. Research indicates that Ast possesses multiple biological functions, including antioxidant, anti-inflammatory, and immune-regulating activities, with therapeutic potential for various chronic diseases such as neurological and cardiovascular disorders.[26] Previous studies have demonstrated the anti-inflammatory effects of Ast polysaccharides in treating kidney stone inflammation by inhibiting proinflammatory signals, such as monocyte chemoattractant protein 1 and interleukin (IL)-6, through the Nrf2–Keap1 signalling pathway.[27] In tissue regeneration, calycosin-7-*O*-β-glucoside, extracted and purified from Ast by PARK scholars, has been shown to induce the production of human mesenchymal stem cells (hMSCs) toward bone differentiation and mineralization through bone morphogenic protein 2–pSmad1/5/8-Wnt3a-pGSK3β and p-AKT pathways, ultimately transcribing to RUNX2.[28] Recent studies have highlighted the significant role played by Ast in immune regulation.[29] In skin damage research performed by Wang *et al.*, when the addition of extracellular vesicles from hMSCs to injured human epidermal cells promoted the secretion of vascular growth factors (vascular endothelial growth factor, fibroblastic growth factor 2, and epithelial growth factor), inflammatory signals (tissue necrosis factor-alpha, IL-1 β, and IL-6) gradually increased until Ast was added, which promoted the recruitment of immune cells and initiated an anti-inflammatory response[30] These findings emphasize the crucial role of Ast in the anti-inflammatory process, particularly in immune regulation.

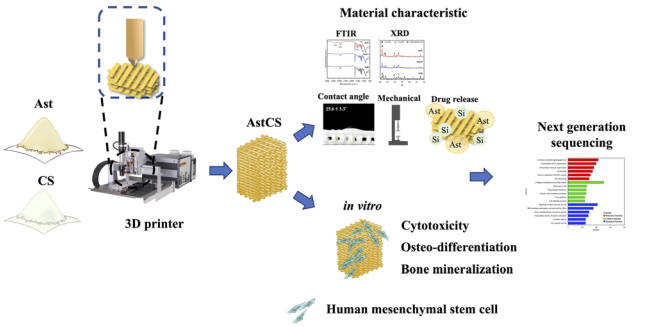

Fig. 1 Illustrative overview of osteogenic enhancement using Ast-infused CS scaffolds, detailing the journey from 3D printing to biological assessment and genetic analysis.

In this study, we investigated the effects of Ast and CS composite scaffolds on hMSCs and examined their potential to promote bone regeneration, vascular neogenesis, and anti-inflammatory effects. The underlying mechanisms were also analyzed. A schematic representation of the osteogenic differentiation enhancement process using Ast and CS scaffold flowchart is shown in Fig. 1. Initially, Ast and CS powders were loaded into a 3D printer. These materials were used to fabricate a composite scaffold, denoted as AstCS. The material characteristics of the scaffold were assessed using Fourier transform infrared spectroscopy (FTIR), X-ray diffraction (XRD), and scanning electron microscopy (SEM). The mechanical properties and drug release profiles of the scaffold were evaluated. Subsequently, the bioactivity of the scaffold was tested *in vitro* using hMSCs by analyzing various properties such as live/dead viability, cytotoxicity, osteogenic differentiation, and bone mineralization. Furthermore, next-generation sequencing, along with Gene Ontology and Kyoto Encyclopedia of Genes and Genomes (KEGG) pathway analyses, was performed to predict potential gene involvement in the process.

2. Materials and methods

2.1 Preparation of the Ast-containing CS powder

In our previous study, CS powder was synthesized using the sintering method.[31] First, the CS powder was fabricated *via* commercial calcium oxide (Sigma-Aldrich, St. Louis, MO, USA), and silicon dioxide (Sigma-Aldrich) with the dopants. Then sintered in a high-temperature furnace at temperatures of up to

© 2024 The Author(s). Published by the Royal Society of Chemistry

Open Access Article. Published on 15 October 2024. Downloaded on 2/12/2026 7:52:48 PM. This article is licensed under a Creative Commons Attribution-NonCommercial 3.0 Unported Licence.

1400 °C at a rate of 10 °C min^{-1} for 2 h. The sintered products were mixed with Ast powder (Biomed, Taichung, Taiwan) and ball-milled at 300 rpm for 8 h by a centrifugal ball mill (Retsch PM100, Germany). Finally, the mixtures were placed in an 80 °C oven for 1 day to obtain powders (AstCS and CS) for subsequent experiments. The specimen codes ''Ast0'', ''Ast2.5'', and ''Ast5'' represent the milled powders obtained by performing Ast concentrations of 0, 2.5, and 5%, respectively.

2.2. Ast ceramic ink preparation and manufacturing of scaffolds

To print the ceramic materials, the ground powders were well dispersed in ethanol to obtain a ceramic suspension using ultrasonication at 100 W for 1 h, followed by the addition of heated polycaprolactone (PCL; molecular weight: 43 000; Polyscience, Warrington, PA, USA) at a bioceramic : PCL ratio of 1 : 1 until the alcohol was completely evaporated. Printable ceramic inks made of PCL-incorporated Ast-doped CS (AstCS) or CS powder (Ast0) were then obtained. A 3D printing system (BioScaffolder 3.1, GeSiM, Grosserkmannsdorf, Germany) was employed for scaffold fabrication, and the printing path was designed using the built-in software. The printing process parameters were as follows: needle size, 400 μm; printing pressure, 200–250 kPa; and printing speed, 1–2 mm s^{-1}. Strut spacing and width were tuned at 0.5 mm according to the printing pressure and speed. With the basic hole structure unchanged, scaffolds of different shapes were printed according to different experimental requirements, as explained in the following subsections.

2.3. Physical and chemical properties of the scaffolds

The phase structure of the scaffold surface was determined using XRD (Shimadzu Corporation, Kyoto, Japan). The conditions were set as follows: divergence of 1° and scatter slits with a receiving slot of 0.10 mm. The scan range was set from 20° to 50° and at θ to 2θ with a scan speed of 1° per min. In addition, functional group changes were detected using the FTIR (Bruker, Germany) with a spectral range of 500–4000 cm^{-1} and a reflection absorption mode of 1 cm^{-1}. The mechanical properties were assessed using the EZ Test machine (Shimadzu, Kyoto, Japan), and the load-bearing conditions of each scaffold were tested at 1 mm min^{-1} until the scaffold fractured. The maximum compressive strength was evaluated based on the recorded stress–strain curves. All trials were performed in six replicates and the values were recorded.

2.4. *In vitro* soaking

The scaffold was immersed in a simulated body fluid (SBF) to determine whether beneficial crystals could be precipitated. The detailed composition of the SBF is as follows; 7.9949 g NaCl, 0.2235 g KCl, 0.147 g K_2HPO_4, 0.3528 g $NaHCO_3$, 0.071 g Na_2SO_4, 0.2775 g $CaCl_2$, and 0.305 g $MgCl_2{\cdot}6H_2O$ in 1000 mL of distilled H_2O. Hydrochloric acid and tris(hydroxymethyl)-aminomethane were then used to control the pH to 7.4. The scaffolds were soaked and removed at various time points. The microstructure of the scaffold surface was investigated using SEM. In addition, Ca and Si ions released into the medium were analyzed using inductive coupled plasma-atomic emission spectrometry (Perkin-Elmer OPT 1MA 3000DV, Shelton, CT, USA).

2.5. Ast release profile

The drug-loaded scaffolds were immersed in phosphate-buffered saline (PBS; pH 7.4) at 37 °C to simulate body conditions. At predetermined time intervals, aliquots of the Ast solution were collected and the amount of the released drug was quantified using an ultraviolet-visible spectrophotometer at 355 nm. Release kinetics were analyzed to determine the release profile and mechanisms.

2.6. Cell adhesion and proliferation

The hMSCs were purchased from Lonza (PT-5025, Lonza, Basel, Switzerland) and grown in a commercially available MSCGM™ Mesenchymal Stem Cell Growth Medium BulletKit™ (PT-3238, Lonza). The medium was replaced with a new culture medium twice a day in a 37 °C humidified atmosphere with 5% CO_2. The experiment was started when the culture reached passages 3–6, the 3D scaffolds were pretreated with 75% ethanol for 1 h. Next, ultraviolet light exposure was performed for 30 min before the cell study. After various culture durations, the PrestoBlue assay (Invitrogen, Carlsbad, CA, USA) was performed following the manufacturer's instructions. Internal mitochondrial activity was investigated based on the color intensity of the reagent. Viability was measured using a multi-well spectrophotometer (Infinite Pro M200; Tecan, Männedorf, Switzerland) at 570 nm with a reference wavelength of 600 nm. A scaffold with human dental pulp stem cell seeding was as used as the control (Ctl) group.

2.7. Cell morphology

Pretreated hMSCs were seeded and cultured on the scaffold for 1 and 3 days, washed three times with PBS (Invitrogen, Carlsbad, CA, USA), and fixed in 4% paraformaldehyde (Sigma-Aldrich, St Louis, MO, USA) for 15 min and then in 0.1% Triton X-100 (Sigma-Aldrich, St Louis, MO, USA) for 15 min at room temperature. Cytoskeletal morphology was observed by F-actin fluorescence by staining the cells with phalloidin conjugated to Alexa Fluor 488 (Invitrogen, Carlsbad, CA, USA) for 1 h. The nuclei were stained with 4′,6-diamidino-2-phenylindole (DAPI; Invitrogen, Carlsbad, CA, USA) for 30 min. PBS washing was performed thrice in each step. Finally, a white light laser confocal microscope (TCS SP8; Leica, Wetzlar, Germany) was used to determine the cell morphology.

2.8. Osteogenesis and inflammation assay

After culturing the hMSCs on the scaffold, the cells were lysed with NP40 and the protein was collected for identifying immune-related and osteogenic-related markers. In the osteogenic assay, the hMSCs were cultured with osteogenesis assay kits (StemPro™ osteogenesis differentiation kit, Invitrogen, Carlsbad, CA, USA) for the estimation of cell differentiation. The expression of alkaline phosphatase (ALP) and osteocalcin (OC) was induced by Ast composite scaffolds on days 3 and 7

Open Access Article. Published on 15 October 2024. Downloaded on 2/12/2026 7:52:48 PM.
This article is licensed under a Creative Commons Attribution-NonCommercial 3.0 Unported Licence.

after cell culture in an osteogenic medium. The cells were lysed with 0.2% NP40 and centrifuged at 6000 rpm for 15 min. ALP activity was determined using p-nitrophenyl phosphate (Sigma-Aldrich) as a substrate. Each sample was mixed with p-nitrophenyl phosphate in 1 mol L^{-1} diethanolamine buffer. Finally, the cells were added to 3 M NaOH to terminate the reaction after 30 min and the absorbance was quantified spectrophotometrically at 405 nm. The quantities of IL-1β, IL-1RA, OPN, and OC (MyBioSource, San Diego, CA, USA) secreted from the hMSCs at different time points were determined using enzyme-linked immunosorbent assay according to the manufacturer's instructions. The concentration of the standard curve was determined through the BCA assay, and a blank well was used as the Ctl group.

2.9. Mineralization

The mineralization capacity of hMSCs was assessed using Alizarin Red S. The cells were seeded on the scaffold and cultured in a commercial osteogenic differentiation medium (StemPro™ osteogenesis differentiation kit, Invitrogen, Carlsbad, CA, USA) for 7 and 14 days. Briefly, the samples were treated with 4% paraformaldehyde (Sigma-Aldrich, St Louis, MO, USA) for 10 min to fix the cell and washed with PBS three times to avoid interference. The cells were stained with 0.5% Alizarin Red S (pH 4.0; Sigma-Aldrich, St Louis, MO, USA) for 15 min. Mineralization images were captured under a metallographic microscope (BX53, Olympus, Tokyo, Japan) to assess Ca deposition.

2.10. RNA sequencing analysis

The total RNA was extracted from clinical tissue samples, tissue-derived cells, and tissue-derived spheroids using a NucleoSpin® RNA Kit (Macherey-Nagel GmbH, Düren, Germany) according to the manufacturer's instructions. The quality, quantity, and integrity of the extracted RNA were evaluated using the NanoDrop1000 spectrophotometer and Agilent 2100 Bioanalyzer (Agilent Technologies, Santa Clara, CA, USA). Samples with RNA integrity of greater than 8.0 were used for RNA sequencing. An mRNA-focused barcoded library was generated using the TruSeq Stranded mRNA Library Preparation Kit (Illumina, San Diego, CA, USA). The libraries were sequenced on the Illumina Nova Seq 6000 platform (Illumina) using 2 × 151 bp paired-end sequencing flow cells according to the manufacturer's instructions. The sequencing data were filtered using SOAPnuke, and a heatmap was drawn using Pheatmap (v1.0.8) according to the gene expression of different samples. Differential expression analysis was performed using DESeq2 (v1.4.5) with a Q value of less than or equal to 0.05. Based on the hypergeometric test, KEGG and GO enrichment analyses of the annotated differentially expressed genes were performed using PhyPer. Using Bonferroni correction, the Q value was used to correct significant levels of terms and pathways with a rigorous threshold (Q value $\leq$ 0.05).

2.11. Statistical analysis

Significant differences were analyzed using one-way analysis of variance for at least three experiments. Statistical comparisons of more than two groups were performed using Scheffé's multiple comparison test. Statistical significance was set at $p < 0.05$.

3. Results and discussion

3.1. Physical and chemical properties of the AstCS scaffold

Fig. 2 shows a composite set of data illustrating the physicochemical changes in the CS scaffolds upon the incorporation of Ast. The functional groups of the CS synthesized using 0%, 2.5%, and 5% of Ast (Ast0, Ast2.5, and Ast5) were analyzed using FTIR spectrophotometry, as shown in Fig. 2A. The infrared spectra were recorded in the wavelength range of 500–4000 cm^{-1}. The spectra revealed characteristic absorption bands at distinct wavenumbers. The broad band at approximately 3261 cm^{-1} is typically attributed to O–H stretching vibrations, indicating the presence of hydroxyl groups or water molecules. The band at 2928 cm^{-1} can be assigned to C–H stretching vibrations, whereas the bands at 1591 and 1087 cm^{-1} correspond to the asymmetric stretching of COO– groups and Si–O–Si asymmetric stretching vibrations, respectively. The peak at 1047 cm^{-1} suggests Si–O stretching in the silicate structure. Modification with Ast appeared to affect the intensity and probably, the position of these bands, suggesting interactions between the scaffold and the biological component, which could lead to changes in the chemical environment of the material. The relatively low intensity of these peaks suggests that the concentration of Ast in the scaffold is low. Although the range of these characteristic peaks is subtle, these results indicate that Astragalus has been successfully incorporated into the CS scaffold. XRD was used to study the interphase patterns, which were

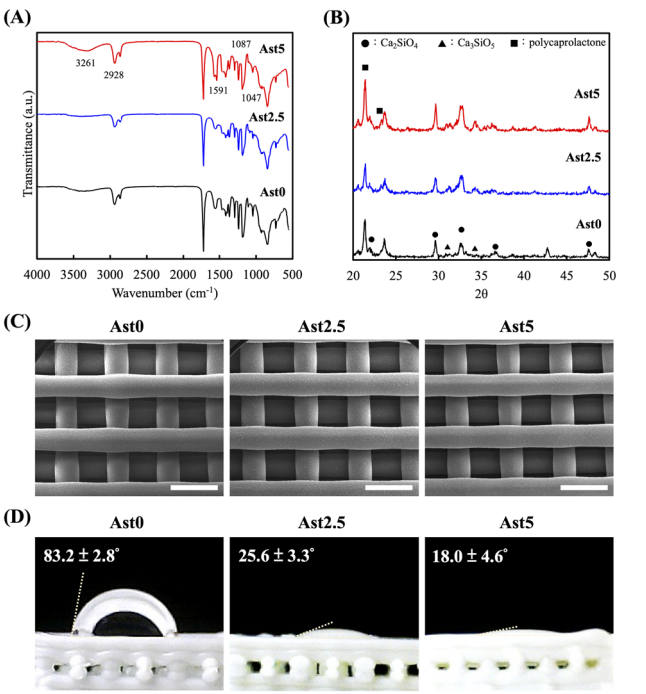

Fig. 2 (A) X-ray diffractometry and (B) Fourier transform infrared spectroscopy. (C) The top view image of the 3D printed scaffold. The scale bar is 1 mm. (D) Contact angle results of the Ast-containing CS scaffolds.

© 2024 The Author(s). Published by the Royal Society of Chemistry

Open Access Article. Published on 15 October 2024. Downloaded on 2/12/2026 7:52:48 PM.
This article is licensed under a Creative Commons Attribution-NonCommercial 3.0 Unported Licence.

important for determining whether Ast was successfully mixed into CS powders. The standard spectra of the Ast scaffolds under various conditions are demonstrated in Fig. 2B. Ast0 exhibited a typical characteristic crystal peak, indicating the presence of a self-crystalline structure. Compared with the Ast0 scaffold, the Ast5 scaffold showed sharp crystalline peaks at $2\theta = 23^\circ$. The spectra of the CS characteristic peak were found at 2θ = 25.4°, 29°, 31.8°, 38.6°, and 49.2°. Ast2 and Ast5 scaffolds had similar Ast peaks at 2θ between 22° to 23°.[32] In this result, while the FTIR spectra of the Ast-incorporated samples show some distinct characteristic peaks compared to pure CS, the relatively low intensity of these peaks can be attributed to the low concentration of Ast in the scaffold. This subtlety in spectral differences, however, does not negate the presence and efficacy of Ast in the composite. To further elucidate the incorporation and functionality of Ast in the scaffolds, biological evaluations such as cell proliferation and anti-inflammation serve as crucial indicators of Ast performance within the scaffold.

SEM of the fabricated AstCS scaffolds is exhibited in Fig. 2C. All the scaffolds had highly specific and controlled structures with pore sizes of approximately 500 μm. Porous scaffolds have always been the center of attraction for bone tissue engineering, as such designs allow scaffolds to support a larger surface area, which is helpful for bone tissue regeneration and integration with surrounding tissues.[33] Various studies have demonstrated the optimal pore sizes for bone tissue regeneration, estimated from 300 to 500 μm. Another important factor to evaluate for macroporous scaffolds is the interconnectivity between pores.[34] The interconnectivity allowed for initial cell adhesion and attachment in addition to initial tissue ingrowth into the center of the scaffolds.[35] In addition, we performed visual and quantitative analyses of the wettability of the scaffold surfaces *via* contact angle measurements as shown in Fig. 2D. The original Ast0 scaffold exhibited a high contact angle of 83.2 ± 2.8°, indicating a relatively hydrophobic surface. Upon the introduction of Ast, a significant reduction in the contact angle was observed for Ast2.5 and Ast5 scaffolds, with values of 25.6 ± 3.3° and 18.0 ± 4.6°, respectively. This drastic decrease in the contact angle with the incorporation of Ast suggests an increase in surface hydrophilicity, which is conducive to cell attachment and proliferation, potentially enhancing the bioactivity and compatibility of the biomaterial.[36] This suggests that Ast retains the structural integrity of Ast0 scaffolds and enhances their surface properties, making them potentially more suitable for biomedical applications.

3.2. Mechanical strength

As shown in Fig. 3A, the scaffolds exhibited different stress–strain behaviours with different Ast concentrations. In particular, Ast5 is significantly different from Ast0, proving that adding a higher concentration of Ast helps improve the overall mechanical properties. The compressive strength values for Ast0 are approximately 4.48 ± 0.40 MPa. Mixing 5% Ast (Ast5) into the calcium silicate significantly increases the compressive strength to around 13.16 ± 0.62 MPa (Fig. 3B). Young's modulus analysis also showed the Ast5 group was 6.0-fold higher

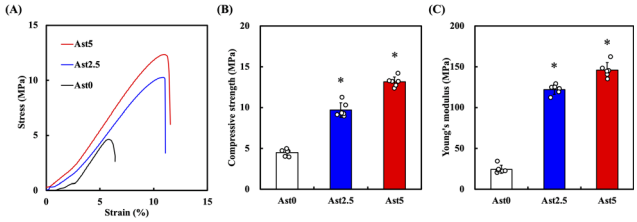

Fig. 3 Mechanical stress analysis of AstCS scaffolds. (A) Stress–strain curve. (B) compressive strength and (C) Young's modulus of Ast0, Ast2, and Ast5 scaffolds. Data presented are n = 6 for each group.

than the Ast0 group and had significant differences (Fig. 3C). These results show that scaffolds modified with Ast are suitable for long-term animal studies and exhibit improved mechanical properties. Several studies have also investigated using other calcium silicate-based scaffolds modified with similar reinforcing agents to enhance mechanical strength. For instance, Leite *et al.* demonstrated that adding chitosan nanoparticles to calcium silicate scaffolds significantly improved compressive strength and Young's modulus.[37] Similarly, Miao *et al.* explored the incorporation of graphene oxide into calcium silicate-based scaffolds, enhancing mechanical properties and improving biocompatibility.[38] These results suggest that scaffolds modified with Ast hold promise for long-term studies within the animal body, with implications for improved mechanical performance and potential applications in tissue engineering and regenerative medicine.

3.3. Bioactivity

To explore whether the AstCS scaffold has bioactive potential, the scaffold was immersed in the SBF to evaluate the apatite precipitate and surface structure. Fig. 4A shows the appearance of AstCS scaffolds under transmission electron microscopy. To understand the changes in the scaffold when implanted in the human body, we conducted a simulated soaking test in the SBF at different time points. SEM images of the surface morphology at intervals of days 0, 1, and 7 for Ast0, Ast2.5, and Ast5 scaffolds were captured. Initially, the Ast0 scaffold exhibited a relatively smooth surface that began to become roughened upon immersion in the SBF, suggesting mineral deposition. On day 1, Ast2.5 and Ast5 scaffolds displayed more pronounced textural changes than the Ast0 scaffold, indicative of enhanced bioactivity. By day 7, the Ast5 scaffold showed a substantial mineral-like layer, which could indicate a scaffold surface that is more conducive to cell attachment and proliferation owing to its increased roughness and surface complexity. The XRD patterns of Ast2.5 and Ast5 scaffolds revealed characteristic peaks of apatite at 26°, 32.5°, and 33.5° (Fig. 4B).[39] Hydroxyapatite possesses excellent bone conductive properties and promotes bone cell integration and regeneration during bone repair. This observation suggests the potential suitability of Ast2.5 and Ast5 scaffolds for bone-related applications owing to hydroxyapatite crystalline peaks.

Therefore, it was necessary to investigate the secretion level of the Ast scaffold over a 28-day period. The ion expression

Open Access Article. Published on 15 October 2024. Downloaded on 2/12/2026 7:52:48 PM.
This article is licensed under a Creative Commons Attribution-NonCommercial 3.0 Unported Licence.

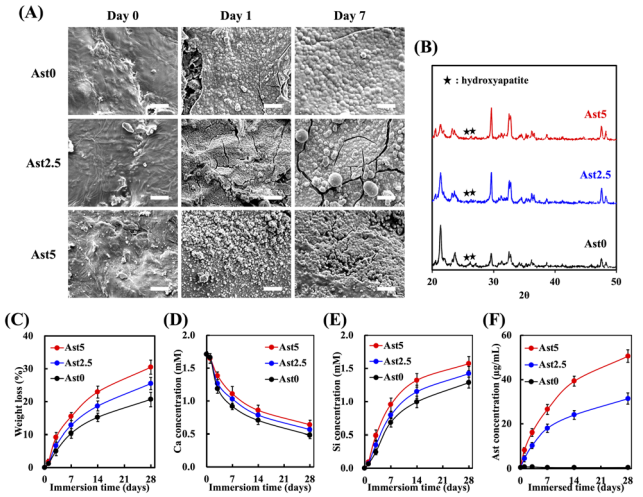

Fig. 4 Surface microstructure of (A) Ast0, Ast2, and Ast5 scaffolds before and after immersion in the SBF for 1 and 3 days observed using scanning electron microscopy. The scale bar is 1 μm. (B) Hydroxyapatite expression of Ast scaffolds. (C) Weight loss percentage of Ast0, Ast2.5, and Ast5 scaffolds over 28 days of immersion. (D) Ca ion concentration changes in SBF solution over 28 days of immersion for Ast0, Ast2.5, and Ast5 scaffolds. (E) Si ion concentration changes in SBF solution over 28 days of immersion for Ast0, Ast2.5, and Ast5 scaffolds. (F) Ast ion concentration changes in SBF solution over 28 days of immersion for Ast0, Ast2.5, and Ast5 scaffolds.

levels of Ca, Si, and Ast demonstrated similar trends, as shown in Fig. 4D and F. The weight loss percentage graph suggests a sustained-release profile, with the Ast5 scaffold showing the highest cumulative weight loss. This might be attributed to a more rapid dissolution or degradation process, which could be advantageous for drug delivery applications where the controlled release of bioactive compounds is desired (Fig. 4C).[40] In addition, the Ca and Si ion concentration graphs exhibited an initial rapid release followed by a plateau, showing a release profile desirable for stimulating local bioactivity without causing systemic effects. The Ast5 scaffold demonstrated the highest release of both ions, which aligned with the more pronounced surface changes observed in the SEM images. Fig. 4F shows that the Ast concentration in the SBF steadily increased over time, with the highest values observed for the Ast5 scaffold. Scanning at full wavelength with different concentrations confirmed the presence of Ast in the scaffolds. Subsequently, the Ast-releasing scaffolds were immersed in a biomimetic fluid for 14 days, and the cumulative release of Ast was analyzed at different time points. The results revealed that the release concentrations of the Ast5 scaffold concentrations that increased rapidly over a short period. The release concentration was 3.16 μg on day 1, increased to 11.06 μg on day 4 and 23.13 μg by day 7, and reached 37.05 μg by day 14. The concentration further increased to 43.39 μg by day 28, representing an approximately 23% increase compared with that of the Ast2.5 scaffold. This suggests that, within 1 month, the composite scaffold not only demonstrated excellent growth factor–carrying capacity but also underwent controlled degradation, facilitating bone tissue regeneration while slowly releasing growth factors.[41]

3.4. Cell proliferation of hMSCs cultured on AstCS scaffolds

To understand the cell adhesion properties of the scaffold and assess the cytotoxicity of the material, phalloidin and DAPI staining was used to evaluate the activity of hMSCs on the composite scaffold. Quantitative assessment of cell proliferation on the scaffolds over culture periods of 1, 3, and 7 days (Fig. 5A). hMSCs in the Ctl, Ast0, Ast2.5, and Ast5 groups showed an increasing trend in absorbance, which correlated with cell growth. Notably, the Ast5 group exhibited a significantly higher absorbance than the Ctl and other groups, particularly on days 3 and 7, suggesting that enhanced cell proliferation could be attributed to a higher Ast content. Confocal microscopy revealed that cells in the Ast5 group exhibited excellent adhesion capabilities on the third day. By the seventh day, these cells were uniformly distributed on the scaffold and displayed tight adhesion with the highest green fluorescence intensity (Fig. 5B). In a previous study, Zhang *et al.* demonstrated that Ast extracts promoted the proliferation and osteogenic differentiation of bone marrow mesenchymal stem cells.[42] The researchers attributed this effect to the upregulation of osteogenic genes and the activation of the Wnt/β-catenin signaling pathway by Ast components.[43] This suggests that the inclusion of Ast in the composite scaffold may promote hMSC proliferation and potentially enhance their osteogenic differentiation, which is crucial for bone tissue regeneration.[44] Furthermore, Ast has been reported to possess angiogenic properties. Wang *et al.* revealed that Ast extracts stimulated angiogenesis both *in vitro* and *in vivo* through the upregulation of vascular endothelial growth factor (VEGF) expression and the promotion of endothelial cell proliferation and tube formation.[45] Some studies have also pointed out that AST can effectively promote angiogenesis.[46] Considering the importance of angiogenesis in tissue regeneration, incorporating Ast in the composite scaffold may contribute to forming functional vascular networks within the

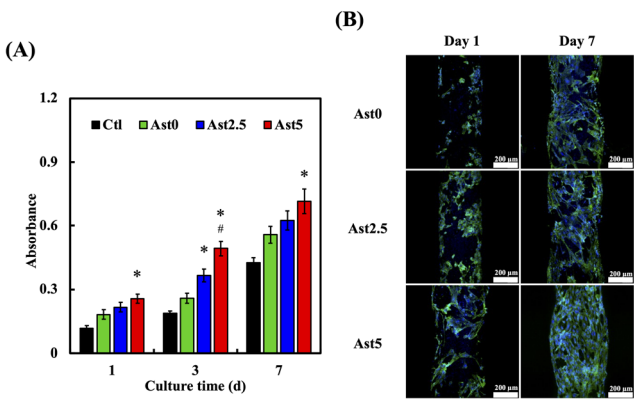

Fig. 5 Cellular proliferation and morphology of Ast-incorporated calcium silicate scaffolds. (A) MTT assay absorbance indicating cell proliferation on scaffolds without Ast0, Ast2.5, and Ast5 compared with the control (Ctl) over 1, 3, and 7 days of culture. Significant differences from the control group are indicated by * for $p < 0.05$ and # for $p < 0.01$. (B) Fluorescence microscopy images display the cellular morphology and density at days 1 and 7 after seeding in different scaffold groups. Cells are stained for actin (green) and nuclei (blue). Scale bar represents 200 μm.

© 2024 The Author(s). Published by the Royal Society of Chemistry

Open Access Article. Published on 15 October 2024. Downloaded on 2/12/2026 7:52:48 PM.
This article is licensed under a Creative Commons Attribution-NonCommercial 3.0 Unported Licence.

engineered tissue, thereby improving its overall viability and integration upon implantation. This trend was significantly more pronounced than in the Ast2.5 and Ast0 groups. This indicated that Ast retained its biological activity and provided a favourable environment for cell growth on the scaffold after 3D printing.

3.5. Inflammatory cytokine analysis

The levels of inflammatory cytokines, including IL-1β, IL-6, and IL-1 RA, were analysed to evaluate the inflammatory response. As illustrated in Fig. 6A, IL-1β concentration was significantly reduced in the Ast5 group compared to the Ctl, Ast0, and Ast2.5 groups after one and three days of culture ($P < 0.05$). Similarly, IL-6 levels (Fig. 6B) were lower in the Ast5 group than in the other groups at both time points ($P < 0.05$). This reduction in proinflammatory cytokines suggests the potential of Ast-containing scaffolds to mitigate inflammation in the context of tissue engineering.[47] Conversely, the anti-inflammatory cytokine IL-1 RA (Fig. 6C) showed significantly higher expression in the Ast5 group than in the other groups after 1 and 3 days of culture ($P < 0.05$). The elevated levels of IL-1RA further support the hypothesis that the Ast-containing scaffolds possess anti-inflammatory properties. This anti-inflammatory effect is crucial because inflammation can impair tissue regeneration and the integration of bone grafts. The results indicate that increasing the Ast content in the scaffolds enhances their anti-inflammatory capabilities, with Ast5 demonstrating the most pronounced effect in modulating cytokine levels.[48] The maintenance of Ast's bioactive properties, particularly its anti-inflammatory effects, underscores the success of our incorporation method. It suggests that the integration process we employed effectively preserves the structural integrity and functional aspects of Ast, allowing it to exert its beneficial effects within the scaffold microenvironment. This outcome not only validates our approach but also emphasizes the potential of Ast as a valuable component in enhancing the biological performance of CS-based scaffolds, especially in contexts where modulation of inflammatory responses is crucial.

3.6. Osteogenic differentiation and mineralization

Bone regeneration is fundamentally connected to osteogenic differentiation and bone mineralization, which are essential for the effective restoration and functional recovery of bone tissue.

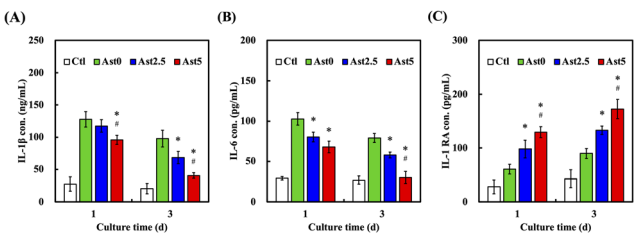

Fig. 6 Effects of Ast-containing scaffolds on inflammatory cytokine expression *in vitro*. The concentrations of (A) IL-1β, (B) IL-6, and (C) IL-1 RA were measured by ELISA in the culture medium of cells grown on different scaffolds. Data are presented as mean ± standard deviation ($n = 3$). *$P < 0.05$ compared to Ctl group; # < 0.05 compared to Ast0 group.

We further investigated whether the AstCS scaffold promotes stem cell differentiation and mineralization. Fig. 7A delineates the ALP activity across various groups. When juxtaposed with Ctl and Ast0, the Ast5 group demonstrated a pronounced increase in ALP activity, which was statistically significant at both 3 and 7 days of culture. The elevation in ALP activity in the Ast5 group than in the Ast2.5 group suggests a dose-dependent enhancement of osteogenic differentiation, positioning Ast5 as the leading scaffold for promoting the early stages of bone formation. The other crucial bone differentiation-related marker, osteocalcin expression (OC), as shown in Fig. 7B, where the Ast5 group exhibited a substantial increase in protein expression compared with the Ast0 and Ast2.5 groups at both 7 and 14 days of culture, underscores its superior mineralization capacity. Various studies have indicated that additives in CS-based scaffold can promote the osteogenic activity of bare scaffold.[49,50] Alizarin Red staining revealed a noticeable increase in the degree of mineralization on the surface of the Ast5 scaffold on days 7 and 14 of cultivation (Fig. 7C). Alizarin Red S staining has emerged as a pivotal technique in assessing bone mineralization, as be an indispensable in bone tissue engineering and regenerative medicine, facilitating the assessment of novel biomaterials and their capacity to promote osteogenic differentiation and bone formation.[17] Our results showed the scaffold colour became increasingly golden, indicating

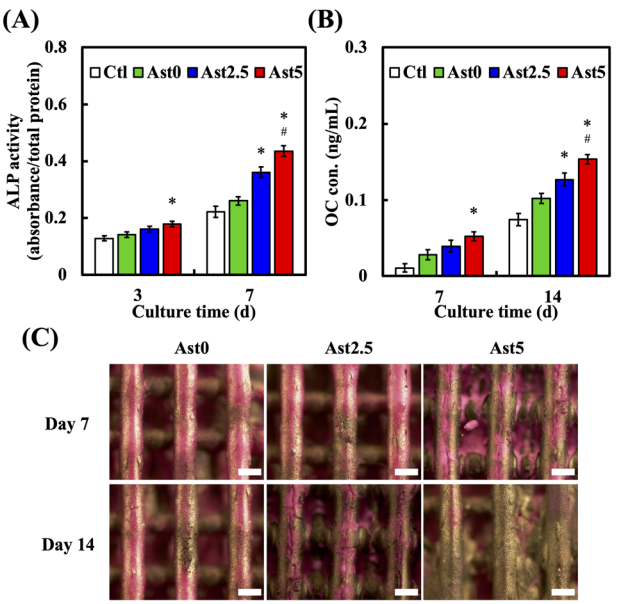

Fig. 7 Osteogenic differentiation and mineralization on AstCS scaffolds. (A) Alkaline phosphatase (ALP) activity normalized to the total protein content, demonstrating early osteogenic differentiation on scaffolds at 3 and 7 days of culture. (*$p < 0.05$ and #$p < 0.01$ compared with Ctl). (B) Quantification of calcium deposits, a marker for bone mineralization, at 7 and 14 days. The Ast5 group shows increased mineralization, as evidenced by higher calcium concentrations (*$p < 0.05$ and #$p < 0.01$ compared to Ctl). (C) Alizarin Red S staining of the scaffolds at days 7 and 14, visualizing the extent of mineral deposition. Increased staining intensity in the Ast5 group correlates with the quantitative calcium deposit data. Scale bars represent 200 μm.

Open Access Article. Published on 15 October 2024. Downloaded on 2/12/2026 7:52:48 PM. This article is licensed under a Creative Commons Attribution-NonCommercial 3.0 Unported Licence.

regions undergoing mineralization. This anthraquinone dye typically forms a vivid red complex with calcium ions, enabling both qualitative and quantitative analysis of mineralized nodules. This colour shift could be attributed to ingredients in Ast interacting with the calcium silicate and Alizarin Red S, potentially forming a unique complex. The golden coloration, while diverging from the typical red, still indicates regions of mineralization. The Ast0 scaffold group also exhibited mineralization-promoting effects but at a slower rate. hMSCs on the Ast5 scaffold displayed mineralized nodules.[51] This finding implies a close association between bone regeneration, reinforcing the notion that Ast5 may aid in bone repair.

3.7. Transcriptome analysis shows that AstCS scaffolds stimulate hMSCs to regulate bone regeneration

As shown in Fig. 8, several genes commonly expressed during bone regeneration were highly expressed in the Ast5 group. These included genes associated with wound healing, focal adhesion, cytokine-mediated signaling pathways, and cytokine activity. These elements play crucial roles in the tissue regeneration and repair processes and act synergistically. The analysis of related pathways using KEGG revealed associations with the MAPK and PI3K/AKT signalling pathways, which are essential for bone regeneration.[52,53] Furthermore, among the significantly differentially expressed genes in the volcano plot between Ast5 and Ast0 (Fig. 8B), we identified key microRNAs related to bone regeneration, angiogenesis, and anti-inflammatory activity. High potential regeneration genes such as E2F transcription factor 2 (E2F2) and aquaporin 3 (AQP3) were expressed in all three processes. E2F2 is a member of the E2F family of transcription factors that plays a critical role in regulating the cell cycle and cellular proliferation (Fig. 7C and D).[54] According to previous reports, these genes play crucial roles in promoting bone formation, angiogenesis, and anti-inflammatory activity (Fig. 8E–G). Studies have demonstrated that E2F transcription factors, including E2F2, can influence the expression of genes involved in immune response and inflammation. For instance, E2F2 has been observed to modulate the expression of cytokines and inflammatory mediators in various cell types, suggesting its possible role in inflammatory processes. However, the specific mechanisms by which E2F2 exerts its anti-inflammatory effects are not well understood and require further investigation.[55] The results showed that AstCS accelerated bone differentiation-related gene expression, suggesting that Ast may exert extraordinary anti-inflammatory effects by recruiting immune cells to contribute to bone-related gene secretion. AQP3 is a member of the aquaporin family of water channel proteins and is predominantly expressed in the kidneys, lungs, and skin. Studies have indicated that AQP3 may play a role in the modulation of inflammatory responses.[56] For example, AQP3 deficiency has been associated with an increased susceptibility to skin dryness and inflammation, indicating its protective role in inflammatory conditions. Furthermore, studies have shown that AQP3 can influence the migration of immune cells and the production of inflammatory cytokines, suggesting its involvement in anti-inflammatory mechanisms.[57] Although no direct evidence suggests that AQP3 can directly promote bone regeneration, numerous studies have indicated that AQP3 can accelerate wound healing. It is reasonable to hypothesize that, in such an environment, AQP3 may also indirectly facilitate the repair of bone defects and angiogenesis, thereby creating a conducive microenvironment for rapid wound closure. In subsequent studies, we will attempt to perform repair tests using extracellular vesicles from stem cells carrying either E2F2 or AQP3.

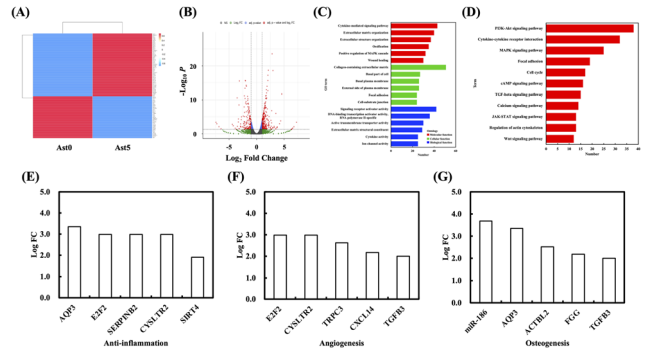

Fig. 8 Relevant transcriptome analysis between Ast5 and Ast0 scaffolds observed in hMSCs. (A) Heatmap, (B) volcano, (C) GO gene expression, (D) KEGG and (E)–(G) images showing significant differences at potential gene levels involved in anti-inflammatory activity, bone regeneration, and angiogenesis.

4. Conclusion

In this study, Ast was combined with CS and successfully printed to form 3D scaffolds. The 3D-printed scaffold had a homogeneous pore morphology and uniform porous structure and demonstrated rapid hydroxyapatite formation after immersion in the SBF solution. Notably, the compressive strength of the scaffolds significantly increased with Ast modification. Our results demonstrated that Ast5 scaffolds exhibited superior mechanical strength, 3.6-fold higher than both the control group and Ast0 scaffolds. We postulate that Ast5 scaffolds possess mechanical properties akin to cortical bone, coupled with favorable degradation characteristics and sustained release of Astragalus. This unique combination facilitates hMSC infiltration, concurrent osteogenic differentiation and mineralization, while promoting angiogenesis, bone regeneration, and anti-inflammatory effects. Previous studies have emphasized the critical role of angiogenesis in bone regeneration efficiency, as it supports bone marrow cavity formation and osteoblast recruitment even inner medullary nerves in defect areas.[58,59] Although Ast0 scaffolds demonstrated some bone tissue regeneration, the expression of osteogenic genes was significantly lower compared to Ast5. Transcriptome analysis predicted potential genes involved in hMSC proliferation when cultured with Ast scaffolds. These findings strongly indicate that 3D-printed AstCS scaffolds have great potential for bone tissue engineering, showcasing an innovative approach that combines advanced biomaterials

© 2024 The Author(s). Published by the Royal Society of Chemistry

Open Access Article. Published on 15 October 2024. Downloaded on 2/12/2026 7:52:48 PM. This article is licensed under a Creative Commons Attribution-NonCommercial 3.0 Unported Licence.

and technology with existing treatment methods to maximize bone regeneration benefits.

Author contributions

J. J. L. and Y. H. L: methodology, validation, investigation, formal analysis, and writing – original draft preparation; T. Y. K. and K. X. L: helped with data analysis and interpretation; C. Y. C. and M. Y. S: funding acquisition and writing – review & editing.

Data availability

The data that support the findings of this study are available from the corresponding author, upon reasonable request.

Conflicts of interest

The authors declare no conflict of interest.

Acknowledgements

The work was supported by the National Science and Technology Council (NSTC 112-2628-E-039-001-MY3, 113-2314-B-039-005, 113-2314-B-039-018, and 111-2314-B-039-082) of Taiwan and China Medical University Hospital Grants (DMR-113-100) of Taiwan. Experiments and data analyses were performed in part by the Medical Research Core Facilities, Office of Research & Development, China Medical University, Taichung, Taiwan.

References

1 X. Sheng, C. Li, Z. Wang, Y. Xu, Y. Sun, W. Zhang, H. Liu and J. Wang, *Mater. Today Bio*, 2023, **20**, 100636.
2 Z. Liu, X. He, S. Chen and H. Yu, *Ceram. Int.*, 2023, **49**, 19355–19363.
3 Q. Liu, W. F. Lu and W. Zhai, *Biomater. Adv.*, 2022, **134**, 112578.
4 Y. Xu, H. Lin, Z. Gao, R. Guo, Y. Kan, L. Han, W. Bu, Z. Wang, A. Asilebieke, L. Han, C. Li, F. He and J. Chu, *J. Mater. Chem. B*, 2024, **12**, 4389–4397.
5 Y. Gu, Y. Zou, Y. Huang, R. Liang, Y. Wu, Y. Hu, Y. Hong, X. Zhang, Y.-C. Toh, H. Ouyang and S. Zhang, *Biofabrication*, 2024, **16**, 015003.
6 H. Shao, J. Zhu, X. Zhao, P. Xia, Y. Wang, T. Zhang, Y. Gong, Y. He and Q. Yao, *Ceram. Int.*, 2024, **50**, 9280–9292.
7 G. A. N. Atia, S. Z. Mohamed, H. A. Halim, M. M. Ghobashy, T. Foda, H. K. Shalaby, M. K. Kundu, M. R. Islam, P. Tagde, N. K. Shaikh, N. Taymour and F. S. Khan, *Ceram. Int.*, 2024, **50**, 22184–22208.
8 S. Luo, Z. Wang, J. He, G. Tang, D. Yuan, Z. Wu, Z. Zou, L. Yang, T. Lu and C. Ye, *Ceram. Int.*, 2024, **50**, 18275–18283.
9 J. Xu, J. Vecstaudza, M. A. Wesdorp, M. Labberté, N. Kops, M. Salerno, J. Kok, M. Simon, M.-F. Harmand, K. Vancíková, B. van Rietbergen, M. M. Misciagna, L. Dolcini, G. Filardo, E. Farrell, G. J. V. M. van Osch, J. Locs and P. A. J. Brama, *Mater. Today Bio*, 2024, **25**, 100959.
10 Ö. Demir, A. Pylostomou and D. Loca, *Biomater. Adv.*, 2024, **157**, 213731.
11 T. Wu, T. Lu, H. Shi, J. Wang and J. Ye, *Ceram. Int.*, 2023, **49**, 6630–6645.
12 C. C. Ho, Y. W. Chen, K. Wang, Y. H. Lin, T. C. Chen and M. Y. Shie, *J. Mater. Chem. B*, 2023, **11**, 72–82.
13 M. Y. Shie and S. J. Ding, *Biomaterials*, 2013, **34**, 6589–6606.
14 Y. C. Chiu, Y. H. Lin, Y. W. Chen, T. Y. Kuo and M. Y. Shie, *J. Mater. Chem. B*, 2023, **11**, 4666–4676.
15 J. Li, J. Li, Y. Wei, N. Xu, J. Li, X. Pu, J. Wang, Z. Huang, X. Liao and G. Yin, *J. Mater. Chem. B*, 2021, **9**, 7848–7865.
16 X. Zhang, J. Cui, L. Cheng and K. Lin, *J. Mater. Chem. B*, 2021, **9**, 3489–3501.
17 Y. H. Lin, K. X. Lee, C. C. Ho, M. J. Fang, T. Y. Kuo and M. Y. Shie, *Biomater. Adv.*, 2022, **135**, 112660.
18 C. T. Kao, Y. C. Chiu, A. K. X. Lee, Y. H. Lin, T. H. Huang, Y. C. Liu and M. Y. Shie, *Mater. Sci. Eng., C*, 2021, **119**, 111629.
19 Y. W. Chen, Y. H. Lin, C. C. Ho, C. Y. Chen, M. H. Yu, A. K. X. Lee, S. C. Chiu, D. Y. Cho and M. Y. Shie, *Biofabrication*, 2024, **16**, 045035.
20 Y. W. Chen, Y. H. Lin, T. L. Lin, K. X. Lee, M. H. Yu and M. Y. Shie, *Biofabrication*, 2023, **15**, 045007.
21 J. E. Hayek, H. Belaid, L. C. de, S. Cyr, G. E. Chawich, E. Coy, I. Iatsunskyi, C. Gervais, J. Elango, C. Zamora-Ledezma, M. Bechelany, M. Nakhl, D. Voiry, P. Miele, M. Zakhour, L. Soussan and C. Salameh, *Mater. Adv.*, 2024, **5**, 3228–3246.
22 C. T. Kao, C. C. Lin, Y. W. Chen, C. H. Yeh, H. Y. Fang and M. Y. Shie, *Mater. Sci. Eng., C*, 2015, **56**, 165–173.
23 Y. L. Tsai, J. J. Lee, C. Y. Wang, Y. H. Lin, C. Y. Chen and M. Y. Shie, *Ceram. Int.*, 2024, **50**, 14656–14663.
24 S. Tan, Y. Qiu, H. Xiong, C. Wang, Y. Chen, W. Wu, Z. Yang and F. Zhao, *Mater. Today Bio*, 2023, **23**, 100843.
25 Z. Wu, Z. Zhong, W. He, Y. Wu, Y. Cai, H. Yang and Y. Hong, *Mater. Adv.*, 2022, **3**, 4295–4309.
26 Y. Du, H. Wan, P. Huang, J. Yang and Y. He, *Biomed. Pharmacother.*, 2022, **147**, 112654.
27 J. Han, D. Guo, X. Y. Sun, J. M. Wang, J. M. Ouyang and B. S. Gui, *Sci. Rep.*, 2019, **9**, 9871.
28 C. X. Li, Y. Liu, Y. Z. Zhang, J. C. Li and J. Lai, *Arch. Pharmacal Res.*, 2022, **45**, 367–389.
29 Y. Zheng, W. Ren, L. Zhang, Y. Zhang, D. Liu and Y. Liu, *Front. Pharmacol.*, 2020, **11**, 349.
30 X. Y. Wang, R. C. Wang, Z. Y. Qu, Y. Z. Zhu and Y. L. Li, *Front. Nat. Prod. Res.*, 2022, **1**, 971679.
31 C. Y. Wang, C. Y. Chen, K. H. Chen, Y. H. Lin, T. P. Yeh, A. K. X. Lee, C. C. Huang and M. Y. Shie, *Ceram. Int.*, 2024, **50**, 7121–7131.
32 T. Lu, J. Wang, X. Yuan, C. Tang, X. Wang, F. He and J. Ye, *Biomater. Adv.*, 2022, **141**, 213120.
33 T. L. Lin, Y. H. Lin, A. K. X. Lee, T. Y. Kuo, C. Y. Chen, K. H. Chen, Y. T. Chou, Y. W. Chen and M. Y. Shie, *Mater. Today Bio*, 2023, **22**, 100728.

© 2024 The Author(s). Published by the Royal Society of Chemistry

Open Access Article. Published on 15 October 2024. Downloaded on 2/12/2026 7:52:48 PM.
This article is licensed under a Creative Commons Attribution-NonCommercial 3.0 Unported Licence.

34 M. J. Kim, J. H. Park, J. M. Seok, J. Jung, T. S. Hwang, H. C. Lee, J. H. Lee, S. A. Park, J. H. Byun and S. H. Oh, *Biofabrication*, 2024, **16**, 025014.
35 K. Y. Chen and C. H. Yao, *Biomedicine*, 2011, **1**, 29–32.
36 F. C. Oliveira, J. O. Carvalho, L. S. S. M. Magalhães, J. M. da Silva, S. R. Pereira, A. L. G. Júnior, L. M. Soares, L. I. C. Cariman, R. I. da Silva, B. C. Viana, E. C. Silva-Filho, S. Afewerki, H. N. da Cunha, M. L. Vega, F. R. Marciano and A. O. Lobo, *Mater. Sci. Eng., C*, 2021, **120**, 111776.
37 M. L. Leite, C. Anselmi, I. P. M. Soares, A. P. Manso, J. Hebling, R. M. Carvalho and C. A. de S. Costa, *Dent. Mater.*, 2022, **38**, 1763–1776.
38 X. Miao, Y. Xing, H. Zheng, Q. Liu, M. Hu and J. Guo, *ACS Omega*, 2023, **8**, 22975–22983.
39 X. Liu, Y. Ma, M. Chen, J. Ji, Y. Zhu, Q. Zhu, M. Guo and P. Zhang, *J. Mater. Chem. B*, 2021, **9**, 6691–6702.
40 P. Ros-Tárraga, C. M. Martínez, M. A. Rodríguez and P. N. D. Aza, *Ceram. Int.*, 2022, **48**, 37114–37121.
41 D. Hu, K. Li, Y. Xie, H. Pan, J. Zhao, L. Huang and X. Zheng, *J. Mater. Sci.: Mater. Med.*, 2016, **27**, 56.
42 Y. M. Zhang, Y. Q. Liu, D. Liu, L. Zhang, J. Qin, Z. Zhang, Y. Su, C. Yan, Y. L. Luo, J. Li, X. Xie and Q. Guan, *Med. Sci. Monit.*, 2019, **25**, 4110–4121.
43 X. Cheng, B. Wei, L. Sun, X. Hu, J. Liang and Y. Chen, *Phytother. Res.*, 2016, **30**, 1680–1688.
44 Y. M. Zhang, L. Y. Zhang, H. Zhou, Y. Y. Li, K. X. Wei, C. H. Li, T. Zhou, J. F. Wang, W. J. Wei, J. R. Hua, Y. He, T. Hong and Y. Q. Liu, *Cell Cycle*, 2020, **19**, 3195–3207.
45 X. Wang, A. F. Valls, G. Schermann, Y. Shen, I. M. Moya, L. Castro, S. Urban, G. M. Solecki, F. Winkler, L. Riedemann, R. K. Jain, M. Mazzone, T. Schmidt, T. Fischer, G. Halder and C. R. de Almodóvar, *Dev. Cell*, 2017, **42**, 462–478.
46 Y. Meng, Y. Zhang, N. Jia, H. Qiao, M. Zhu, Q. Meng, Q. Lu and Y. Zu, *Int. J. Biol. Macromol.*, 2018, **118**, 1438–1448.
47 G. T. Yu, W. X. Zhu, Y. Y. Zhao, H. Cui, H. Chen, Y. Chen, T. T. Ning, M. D. Rong, L. Rao and D. D. Ma, *Biofabrication*, 2024, **16**, 025007.
48 N. O. Monteiro, M. R. Casanova, R. Quinteira, J. F. Fangueiro, R. L. Reis and N. M. Neves, *Biomater. Adv.*, 2022, **141**, 213128.
49 M. Ge, D. Xie, C. Jiao, Y. Yang, L. Shen, M. Qiu, H. Zhang, Z. He, H. Liang and Z. Tian, *Ceram. Int.*, 2022, **48**, 21175–21186.
50 K. Dai, Z. Yang, L. Ding, Z. Yang, F. Hang, X. Cao, D. Chen, F. Zhao and X. Chen, *Ceram. Int.*, 2023, **49**, 19773–19785.
51 J. Wu, C. Jiao, H. Yu, H. Liang, J. Zhao, Z. Tian, C. Wang, L. Shen and D. Wang, *Ceram. Int.*, 2023, **49**, 35438–35447.
52 N. J. N. Nasir, N. Arifin, K. B. A. A. Noordin and N. Yusop, *J. Taibah Univ. Med. Sci.*, 2023, **18**, 1350–1363.
53 J. Dong, X. Xu, Q. Zhang, Z. Yuan and B. Tan, *Exp. Cell Res.*, 2020, **394**, 112137.
54 J. Zhou, M. Cheng, M. Wu, C. Boriboun, K. Jujo, S. Xu, T. C. Zhao, Y.-L. Tang, R. Kishore and G. Qin, *J. Mol. Cell. Cardiol.*, 2013, **60**, 68–71.
55 S. Wang, L. Wang, C. Wu, S. Sun and J. Pan, *Arthritis Res. Ther.*, 2018, **20**, 225.
56 M. Hara-Chikuma, M. Tanaka, A. S. Verkman and M. Yasui, *Nat. Commun.*, 2020, **11**, 5666.
57 I. V. da Silva, A. G. Silva, C. Pimpão and G. Soveral, *Biochimie*, 2021, **188**, 35–44.
58 Y. Li, J. Zhu, X. Zhang, Y. Li, S. Zhang, L. Yang, R. Li, Q. Wan, X. Pei, J. Chen and J. Wang, *ACS Appl. Mater. Interfaces*, 2023, **15**, 17543–17561.
59 M. Lian, Z. Qiao, S. Qiao, X. Zhang, J. Lin, R. Xu, N. Zhu, T. Tang, Z. Huang, W. Jiang, J. Shi, Y. Hao, H. Lai and K. Dai, *ACS Nano*, 2024, **18**, 7504–7520.

© 2024 The Author(s). Published by the Royal Society of Chemistry